Nanotechnology

PAPER

Quality enhancement of low temperature metal organic chemical vapor deposited MoS_2: an experimental and computational investigation

IOP Publishing Nanotechnology
Nanotechnology 30 (2019) 395402 (9pp) https://doi.org/10.1088/1361-6528/ab2c3a

Quality enhancement of low temperature metal organic chemical vapor deposited MoS_2: an experimental and computational investigation

Zahabul Islam[1,2], Kehao Zhang[2,3], Joshua Robinson[2,3] and Aman Haque[1,2,4]

[1] Mechanical Engineering, University Park, PA 16802, The Pennsylvania State University, United States of America
[2] Center for Atomically Thin Multifunctional Coatings (ATOMIC), Center for Two-Dimensional and Layered Materials (2DLM), Materials Research Institute; The Pennsylvania State University, PA 16802, United States of America
[3] Materials Science and Engineering, The Pennsylvania State University, PA 16802, United States of America

E-mail: mah37@psu.edu

Received 21 March 2019, revised 11 June 2019
Accepted for publication 24 June 2019
Published 16 July 2019

Abstract

Electronic quality of chemical vapor deposited MoS_2 is a function of crystallinity, which tends to decline with decrease in deposition temperature. Conventional thermal annealing can improve the quality but requires very high temperatures. In this study, we investigate a novel low temperature (room temperature to 400 °C) annealing process that exploits the electron wind force during passage of current. Here, moderate current density gives rise to atomic scale mechanical force whenever the electrons encounter defects in the lattice or grain boundaries (GBs). After hypothesizing that this force can significantly enhance defect mobility without any temperature field, we demonstrate the process using *in situ* transmission electron microscope and molecular dynamics simulation. Monolayer metal organic chemical vapor deposited MoS_2 deposited at 400 °C was post processed at temperature as low as 20 °C. Experimental results show five times enhancement in electrical conductivity, which is supported by electron diffraction patterns indicating significant grain growth. Discrete spots in diffraction indicate evolution of high crystallinity even at room temperature. Our computational model shows the mechanisms behind healing lattice defects as well as reorienting the GBs. The enhancement in microstructure of the specimen is also reflected in mechanical properties simulations on pre- and post-annealed specimens.

Keywords: two-dimensional materials, molybdenum disulfide, *in situ* transmission electron microscopy, molecular dynamics, low temperature annealing, defects, grain boundary

(Some figures may appear in colour only in the online journal)

1. Introduction

Transition metal dichalcogenide crystals such as MoS_2 in two-dimensional (2D) form show intrinsic band gap ranging from 1.2 to 1.8 eV depending on the number of layers [1]. MoS_2 has attracted the 2D materials community because of their distinctive electrical, optical, and mechanical properties [2–4], making it desirable for field-effect transistors [5–7], flexible electronics [8–10] and sensors [11, 12] applications. Exfoliated MoS_2 layers show the highest quality, however

[4] Author to whom any correspondence should be addressed.

limited flake size and exfoliation-induced defects remain concerns for scalability [13–15]. The need for scalable production of large-area and highly crystalline MoS_2 has spurred advances in chemical vapor deposition (CVD) processes [16–18]. Quality of CVD grown 2D materials is a strong function of deposition temperature. Thus, the quality of low temperature deposited materials can still be enhanced with post-processing annealing. Unfortunately, for MoS_2, the required temperatures for thermal annealing may be in excess of 800 °C [19, 20]. From device fabrication process compatibility perspective, lower temperatures are desired. However, lower temperature deposition is also known to decrease the materials quality. For example, multiple nucleation sites on supporting substrate could lead to the formation of nanocrystalline MoS_2 during the CVD growth, with grains oriented in different directions and connected by grain boundaries (GBs) [21, 22]. GBs in 2D materials have detrimental effects on physical properties such as higher resistivity, lower carrier mobility, poor mechanical properties and lower thermal conductivity of 2D materials [23–28].

The objective of this study is to minimize the defects and GBs in low temperature CVD grown MoS_2. The most commonly used technique is conventional thermal annealing, where high temperature is used to enhance defect mobility to minimize their volume fraction in the solid, or to minimize the GB density (thus increasing the grain size). This has been used for almost all materials in all dimensions. The literature contains evidence of post-synthesis thermal annealing of MoS_2 to enhance the crystallinity through *ex situ* [29] as well as *in situ* [30] experiments. The reported temperature range is 700 °C–1000 °C for annealing time on the hours. The general agreement is that very little improvement in the microstructure is seen below 800 °C. This is not unexpected since MoS_2 is a high temperature solid lubricant material [31]. Very high temperature processes are not desirable in multi-layered electronic devices because of thermal stresses. In addition, thermal annealing takes very long time because highly uniform temperature means random diffusion, where both lattice and defective regions are given equal vibrational energy [32]. These concerns motivate the present study, where the objective is to develop a low temperature and faster processing condition. As described in a later section, our processing temperature was below 400 °C and time was less than 5 min. In this study, we propose that defects in electrically conducting materials can be targeted using a non-thermal process, i.e. momentum transfer of electrons at defects. Here, we apply electrical current in the specimen at moderate current density ($<10^6$ A cm^{-2}). In the lattice, the electron scattering is mostly elastic in nature. However, the scattering is massive at the defects, where the electrons lose the momentum [33], developing atomic scale force known as the 'electron wind force'. Such momentum transfer imparts high defect mobility and creates a 'directional diffusion' (compared to the random diffusion in high temperature heating) because electron flow itself is highly directional (cathode to anode). Our hypothesis is that such directed, non-thermal diffusion can be effectively exploited to control defect mobility and migration at low temperature and high speed. It is important to note that Joule heating always accompanies the electron wind force. Temperature from such resistive heating can be helpful in enhancing defect mobility, so long its inherent randomness in diffusion not dominate the electron wind force effects. In this study, such balance of Joule heating and electron wind force is achieved through careful consideration of specimen geometry and thermal boundary conditions. Our proposed electrical annealing technique is effective for nanocrystalline metallic or semiconducting materials which contain high volume fraction of defects at the GBs. This technique has been also successfully deployed for conductive thin films, additive manufactured materials and alloys [34–36].

In this study, we adopt a combined experimental-computational approach to investigate the proposed electron wind force induced low temperature annealing process. Nominally monolayer MoS_2 specimens are synthesized at 400 °C using MOCVD. The material is then transferred to a custom designed and fabricated micro-electro-mechanical (MEMS) chip that can be accommodated by a TEM specimen holder with electrical biasing capability. The specimen resistance and electron diffraction patterns are recorded for the input current density. Significant enhancement in electronic quality of the specimens was observed through these acquired data. To obtain atomic scale defect mobility and migration mechanisms that lead to low temperature electron wind force induced annealing, we develop MD simulation models using LAMMPS [37] simulation package. Here, the Huntington–Grone model [38] is used to determine the electron wind force that is imposed on the specimen atoms. We also probe the effectiveness of electrical annealing on mechanical properties of pre-annealed and post-annealed sample by conducting tensile testing simulation.

2. Experimental and computational details

2.1. MOCVD synthesis

The low temperature synthesis of MoS_2 is conducted by metal organic chemical vapor deposition (MOCVD), the reactor design and experimental procedures are described elsewhere [39, 40] Briefly, 4×10^{-4} sccm molybdenum hexacarbonyl ($Mo(CO)_6$) and 0.55 sccm diethyl sulfide (DES) were carried to the hot wall MOCVD reactor by 50 sccm H_2 and 565 sccm Ar. The growth is conducted at 400 °C for 1 h on 300 nm SiO_2 substrate that yielded nominally one layer of MoS_2.

2.2. Device fabrication and sample transfer

MoS_2 sample was transferred on the MEMS chip for electrical biasing using PMMA and HF solution. Device design and fabrication details are given elsewhere [41]. Schematic of the transfer technique and experimental setup is shown in figure 1. At first, MoS_2/sapphire specimen is spin-coated with 950 K PMMA A2 at 1500 rpm. After spin coating MoS_2/PMMA is released in 16% HF solution from sapphire utilizing the surface tension to peel off the MoS_2/PMMA film [42]. Then released specimen is captured on the desired

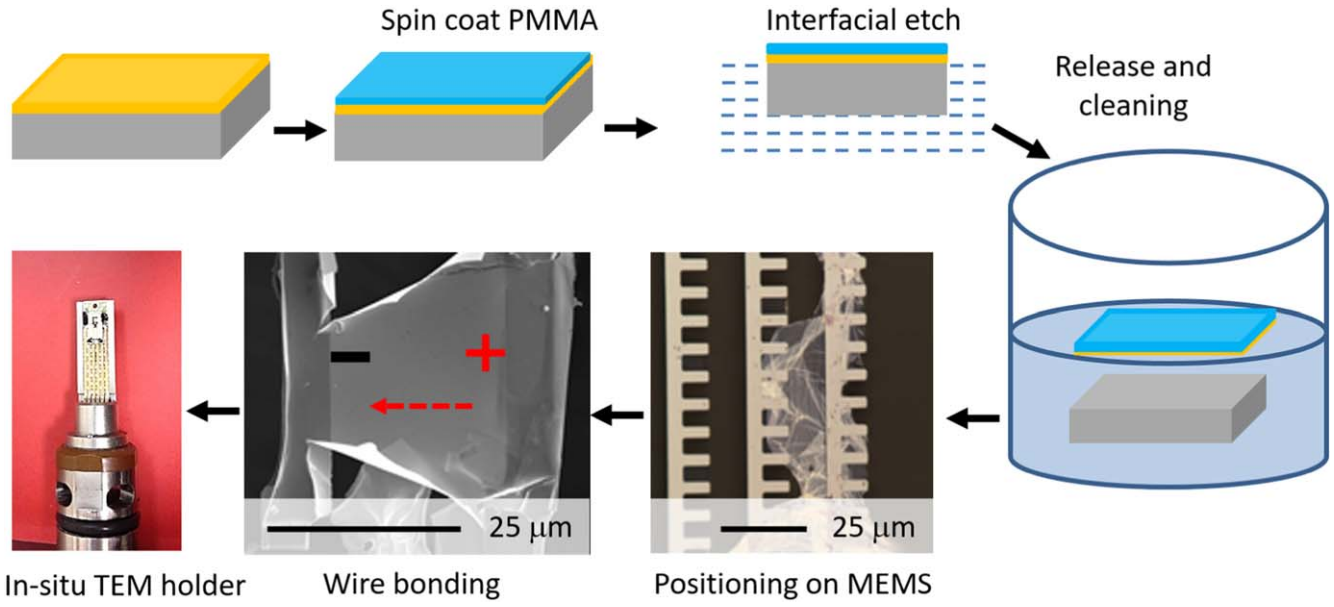

Figure 1. Schematic description of the monolayer MoS_2 transfer process on to a MEMS device and subsequent experimental setup for *in situ* TEM investigation of electrical property as function specimen microstructure.

location of the MEMS device for biasing purpose. Finally, acetone and isopropyl alcohol is used to dissolve PMMA film to obtain freestanding MoS_2 sample. The device is then wire bonded and mounted on a TEM specimen holder.

2.3. Computational details

We developed classical MD simulation model using reactive empirical bond-order (REBO) potential [43] and implemented it in LAMMPS [37]. We modeled single layer polycrystalline MoS_2 with 10 randomly oriented grains with approximate grain size of 2.5 nm using the Voronoi-tessellation method. The model was checked for overlapping of atoms at the GBs. To incorporate both Joule heating and electron wind force effect, we conduct the simulation at different temperatures with an additional imparted electron wind force on each atoms. We used 0.5 fs simulation time step and maintained periodic boundary condition along the length of the sample (i.e. *x*-direction) while keeping free boundary conditions on transverse and film normal directions (i.e. *y* and *z* directions respectively). Energy minimization was performed on the simulation cell using conjugate-gradient method followed by NVT dynamics at 1000 K for several thousand steps in LAMMPS. Time integration was carried out using the Verlet algorithm during the NVT dynamics. The electron wind force was applied on individual atom. It is difficult for a large system to directly employ electron effects in classical MD simulation as classical MD simulation solely depends on Newton's equation of motion. Thus in this present study, we indirectly quantify equivalent wind force on each atom using the Huntington–Grone [38] model. Effectively, this applies an equivalent electron wind force (F_{wind}) on each atom based on the following equations [44]:

$$F_{wind} = Z^* \times e \times j \times \rho, \quad (1)$$

where, Z^* is effective valence number of molybdenum, e is electron charge, j is the current density and ρ is the specific resistivity. Considering experimental current density of 9.5×10^5 A cm^{-2} and using equation (1) calculated electron wind force on individual atom was 0.3 fN (femto Newton). In addition, interatomic force due to the REBO potential (F_{REBO}), individual atom experiences a total force as follows:

$$F_{Total} = F_{\mathrm{REBO}} + F_{wind}. \quad (2)$$

To mimic the experimental condition i.e. direct current (dc) in the specimen, we impart the electron wind force on individual atoms for 1.0 ns.

3. Results and discussion

To investigate the electrical current annealing induced quality enhancement in low temperature MOCVD MoS_2, we conducted both *in situ* TEM (electrical biasing and resistance measuring) experiments and MD simulation. Experiments were performed inside a FEI^{TM} Talos F200X scanning/transmission electron microscope (S/TEM) with a resolution of 0.12 nm using field emission gun and 200 kV acceleration voltage. In our experiments, dc current is passed through the specimen in steps of 10 μA until 0.1 mA limit is reached. Current density which defined as current per unit cross-sectional area was calculated assuming 1 nm thickness of the sample [45]. We allow about 5 min only of anneal time between each current density steps, which is remarkably shorter than conventional thermal annealing. At 0.1 mA, the current density is 9.5×10^5 A cm^{-2}, a value close to the electromigration damage in metallic materials [46]. Figure 2(a) shows a representative specimen resistance versus current density data. Here, the initial resistance is seen to reduce dramatically from 1 MΩ to about 180 kΩ after the electrical annealing. Figure 2(b) shows coupled electro-thermal simulation results estimating the temperature profile in the specimen. In our present simulation, we consider low thermal conductivity of

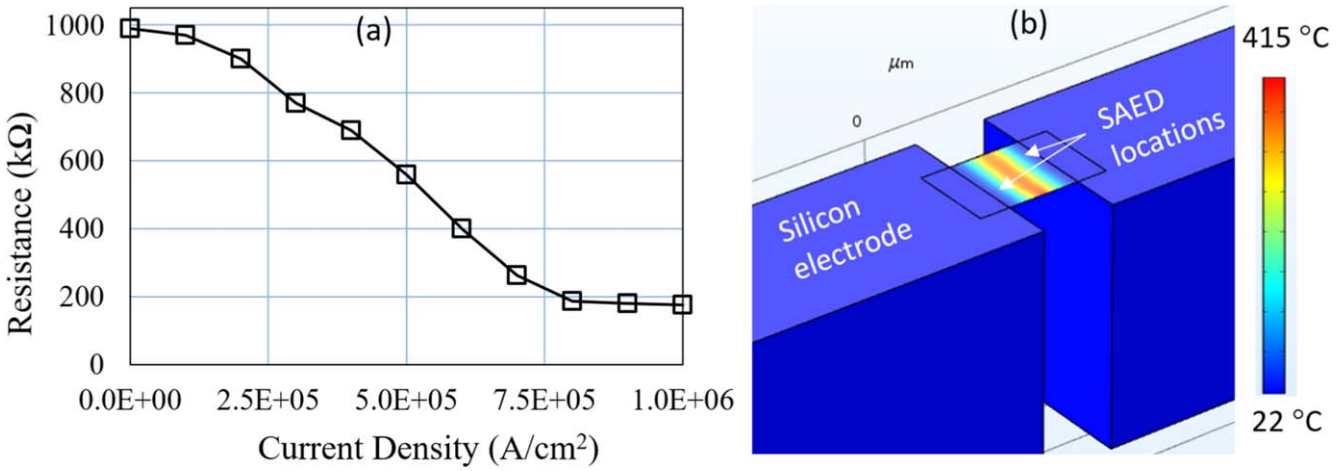

Figure 2. (a) Observation of five times decrease in electrical resistance of nominally MoS_2 specimens during electron wind force annealing. (b) Spatial temperature distribution for the highest current density.

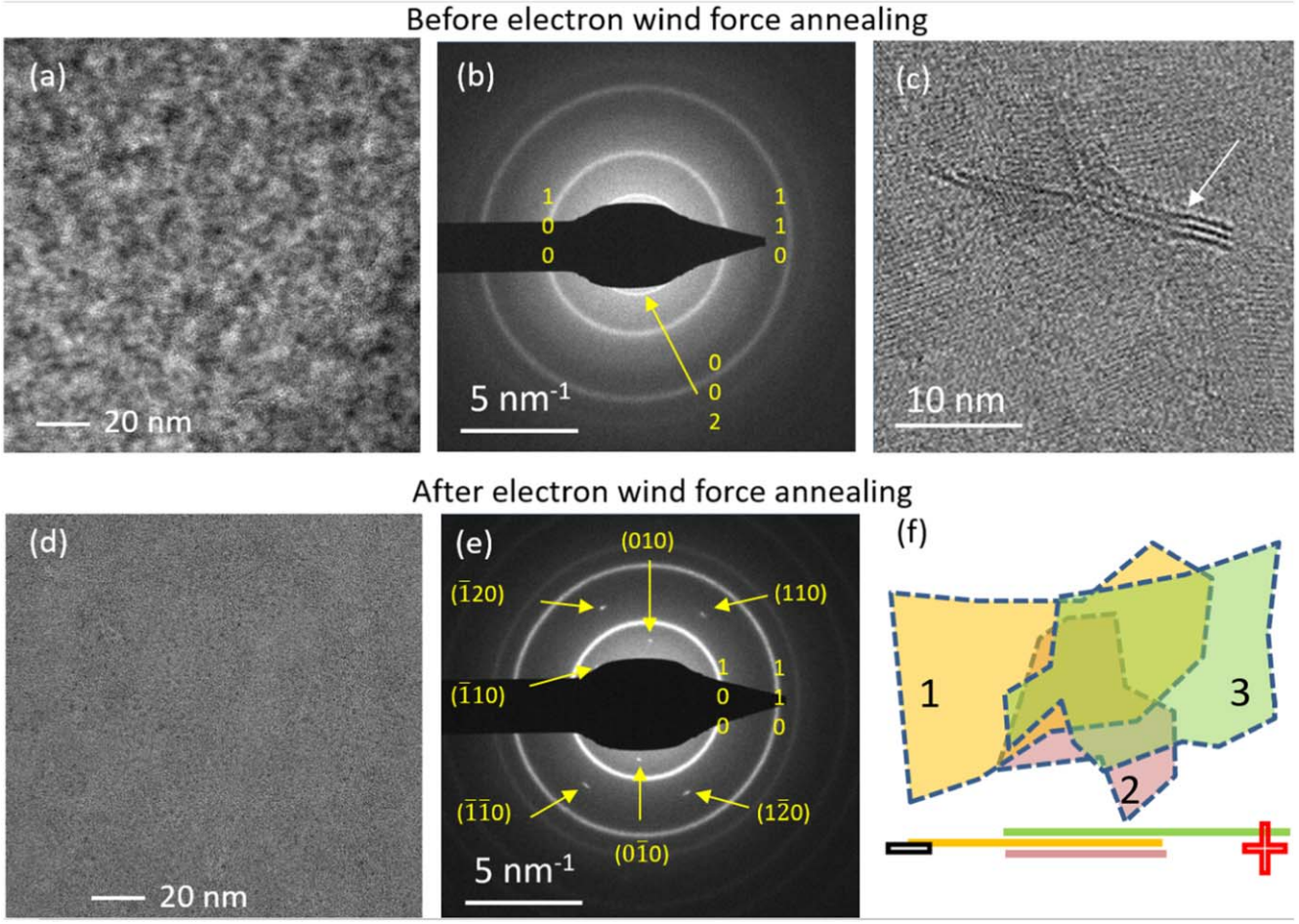

Figure 3. *In situ* TEM electron wind force annealing results (a) bright-field image. (b) SAED pattern from as-deposited monolayer MoS_2 specimen. (c), (d) The same location after application of 9.5×10^5 A cm^{-2} current density at near room temperature, (e) SAED of the same region after electrical annealing. (f) Regions with various atomic layer configurations illustrating possible domains that are not annealed.

MoS_2 [47] to ensure maximum temperature rise during the electrical biasing of MoS_2. Raman thermometry [48] measurement shows that MoS_2 temperature could reach as high as 380 °C prior to their breakdown at a drain current of 210 μA μm^{-1}. The reported electrical current is more than twice in magnitude higher compared to our biasing condition. Thus actual temperature rise in our sample might be even lower than the predicted simulation results. Because of the freestanding geometry, the specimen temperature is the highest (around 400 °C) in a very small section in the middle. The massive

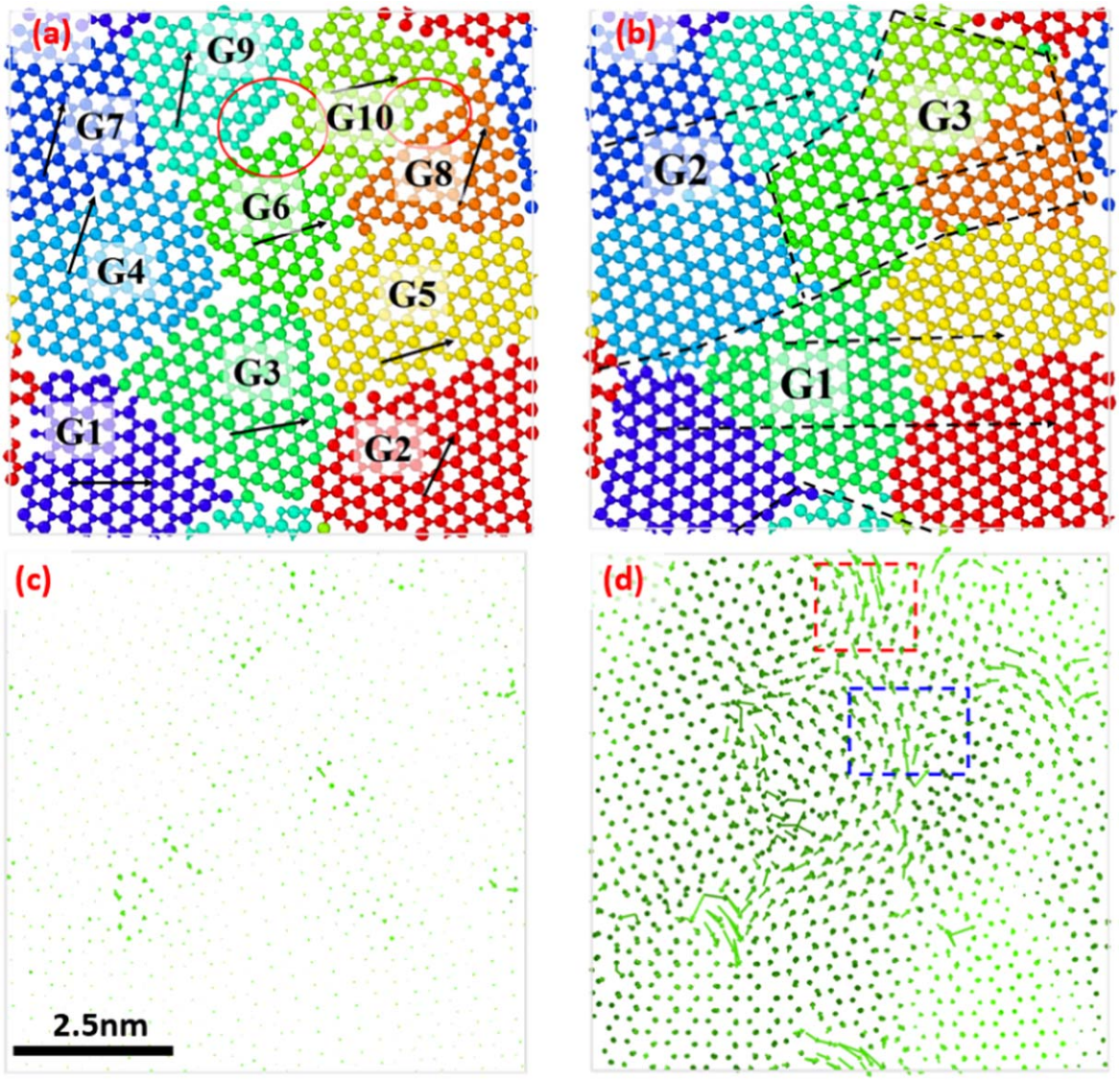

Figure 4. MD simulation results on electron wind force annealing (a) simulation cell showing 10 grains with average size of 2.5 nm before annealing. (b) Same specimen showing three grains with average size of 7 nm after annealing. Displacement vector analysis (c) before annealing. (d) During the annealing. (Individual grains are shown by different colors; smaller radius sphere indicates sulfur atoms and larger sphere indicates molybdenum atoms.)

silicon electrodes effectively constrain the specimen ends to be at room temperature. The arrows in figure 2(b) indicates the locations for the selected area electron diffraction (SAED) patterns. Or in other words, we report the enhancement of crystallinity in regions that are constrained to near room temperature conditions.

To explain the observed reduction in electrical resistance, we note that thin film resistance is strongly influenced by surface and internal (such as GB) defects. Our *in situ* TEM results shed light on the changes in the microstructure as a function of the applied electrical current density. Figures 3(a) and (b) show the bright-field and SAED images for the as-deposited specimen. Figure 3(c) shows TEM bright-field image before electrical annealing. After annealing at near room temperature with electron wind force at 9×10^5 A cm^{-2} current density, the corresponding image is shown in figure 3(d). The transformation to apparent featureless appearance in figure 3(d) suggests significant decrease in surface roughness, which may contribute to the decreased surface scattering. This may have significant impact on the electrical resistance (figure 2(a)) as the surface scattering of electrons plays a dominant role [49] because of the freestanding and ultra-thin nature of our specimen.

Another dominant scattering event takes place in the GBs, which have high volume fraction in our specimens with initial grain size less than 5 nm. This is in agreement with the diffraction patterns available in the literature [20]. Since this is smaller than the average electron mean free path, a small increase in grain size can result in very large decrease in resistance. A representative TEM diffraction pattern at low temperature regions in specimens after electron wind force annealing is shown in figure 3(e). Here, the initially diffused rings appear sharper with annealing. More remarkably, we observe distinct hexagonal spots at a current density of

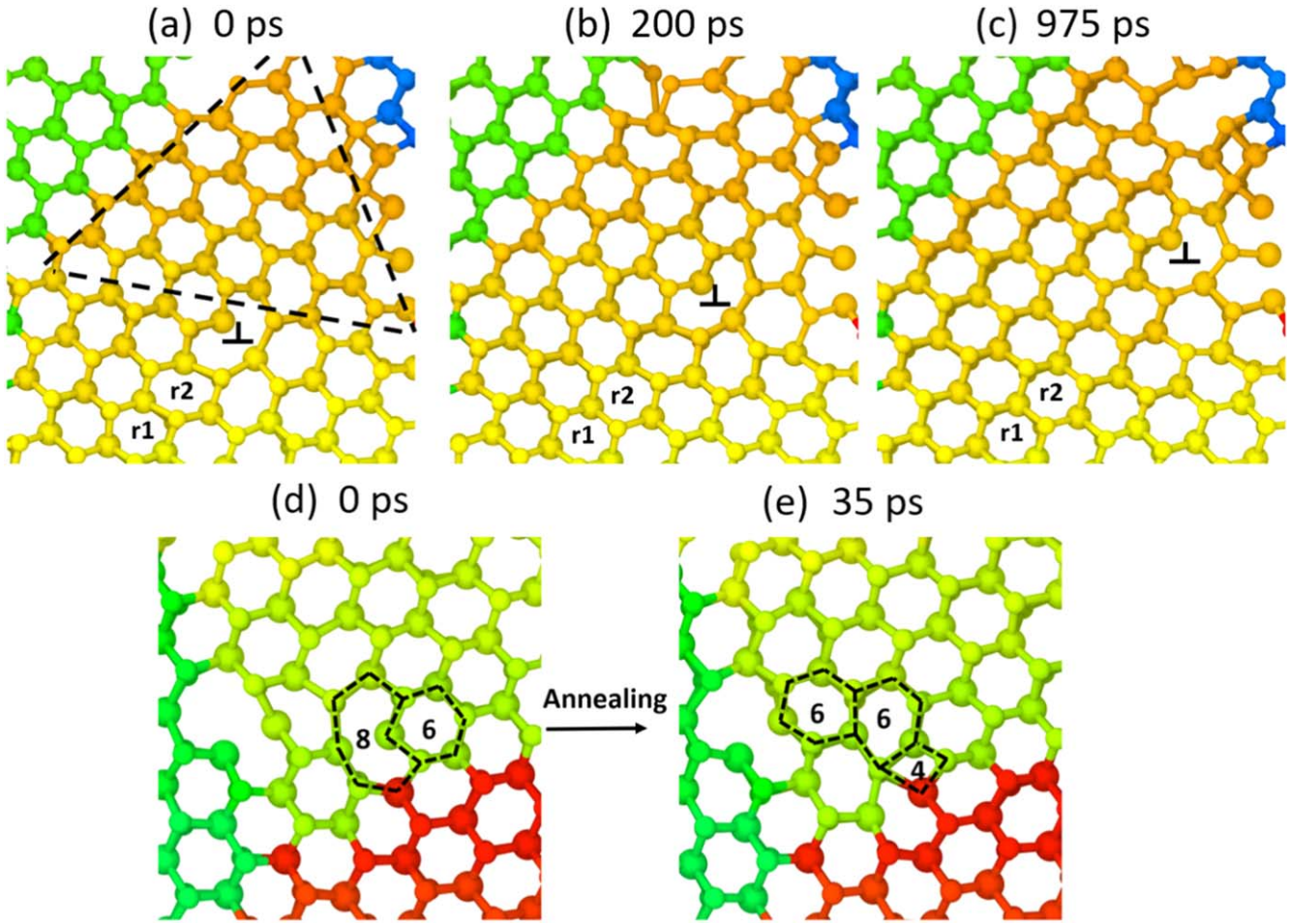

Figure 5. (a)–(c) 6|8Mo Dislocation migration during the electrical annealing. (d)–(e) Transformation of 6|8 ring to 6|6|4 ring at the grain boundary (GB). (Individual grains are shown by different colors, smaller radius sphere indicates Sulfur atoms and larger sphere indicates Molybdenum atoms.)

9.5×10^5 A cm^{-2}, suggesting existence of large crystalline domains alongside or underneath smaller grains. This observation follows the scaling of electron wind force, which is the highest in the GBs. While the discrete spots in the diffraction pattern are unambiguous evidence of large scale highly crystalline domains, the actual description of the annealed specimen morphology is difficult to achieve. There are a few possibilities such as (a) prominent secondary grain growth, where energetically favorable grains may grow abnormally large at the expense of neighboring smaller grains [50] and (b) electrical discontinuity in domains that lead to little annealing effect. Figure 3(f) schematically describes a possible scenario with a region where three atomic layers exist. The existence of such multi-layer configuration is supported by TEM images, as indicated by the arrow in figure 3(e). If layers or domains 1 and 3 are physically connected as shown, and both are laid down on the domain 2, most of the current will flow directly from domain 1–3 or vice versa. The underlaid domain 2 may conduct little or no current at all. In that case, domain 2 will remain un-annealed and any TEM diffraction pattern taken for this ensemble will show sharp spots originating from domains 1 and 3 and diffused rings from domain 2.

To obtain atomic scale understanding of the electron wind force based annealing, we performed a series of MD simulations. The first set of experiments were dedicated to the mobility and migration of GB defects and their consequent elimination from the monolayer specimen, resulting in net growth of the average grain size. Figure 4(a) shows the pre-annealed sample with approximately 2.5 nm grain size containing 10 grains. It important to note that the GB structure of 2D MoS_2 is different from ordinary polycrystalline materials. It contains different types of ring defects such as 6|8, 5|7, 4|6, 4|8 as well as vacancies. The 6|8 ring defects could be generated from the 5|7 ring defects by inserting one molybdenum (Mo) or one pair of sulfur (S) atoms. On the other hand, the 4|8 defects could arise from the 5|7 defects by deleting one Mo or one pair of S atoms [51, 52]. We also notice that the 6|8 ring defects could be transformed to two perfect 6 rings and one 4 ring defects i.e. 6|6|4. As shown in figure 4(a) initial grains are randomly oriented. The large density of defects at the GBs is clearly visible and two examples are marked with ovals. Figure 4(b) shows the post-annealed sample after 1.0 ns dynamics run, where the boundaries of 10 grains restructured to three grains with average size of ~7 nm. This indicates that equivalent electron wind force imparted on the sample can

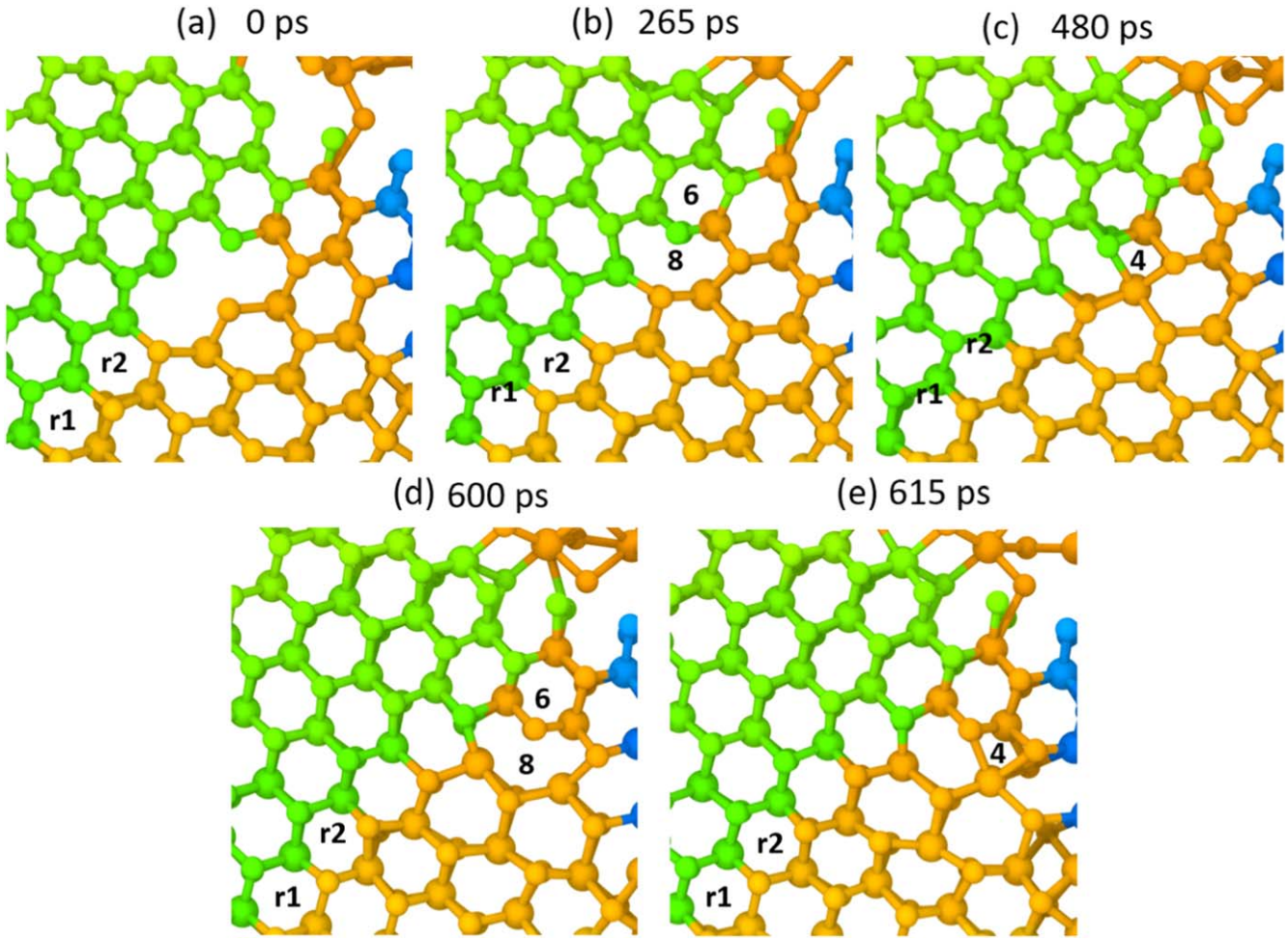

Figure 6. Transformation of vacancy defects to 6 and 4 ring defects at the GB (a) vacancy defects at the GB. (b) Vacancy transforms to 6|8 S defects. (c) 6|8 S Transforms to 6|6|4 ring defects. (d) Formation of 6|8 S due to the dislocation motion. (e) Formation of 6|6|4 ring. (Individual grains are shown by different colors, smaller radius sphere indicates sulfur atoms and larger sphere indicates molybdenum atoms.)

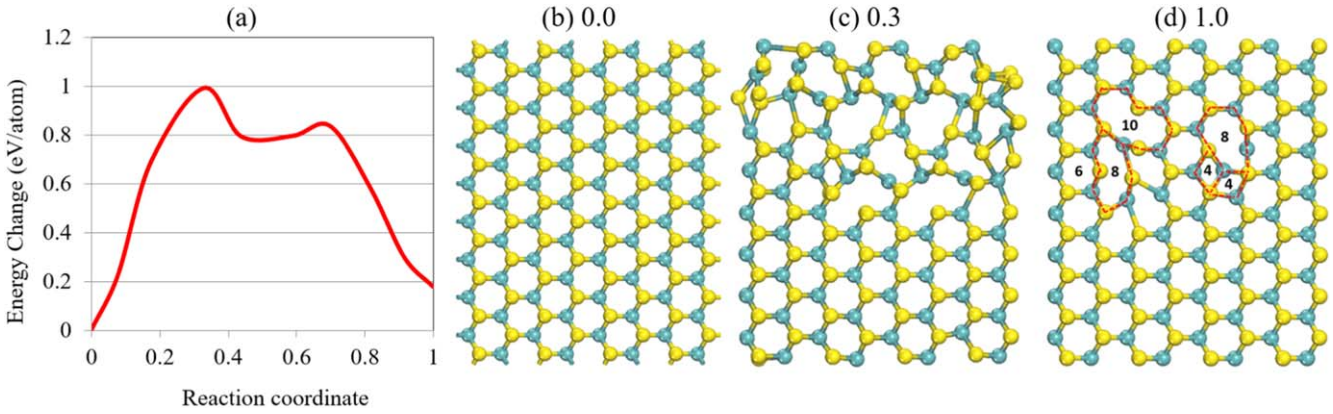

Figure 7. (a) Energy barrier plot. (b) Pristine MoS_2. (c) Intermediate structure at reaction coordinate 0.3 during NEB calculation. (d) defective MoS_2.

effectively mobilize and migrate the defects in the GB. Figures 4(c) and (d) show displacement vector of the pre-annealed and post-annealed sample respectively. Electrical current annealing induces both GB sliding and rotation at the GBs' atoms as shown in figures 4(c) and (d). In figure 4(d), the dotted blue and red color boxes indicate sliding and rotation motion of GBs' atom respectively.

To investigate the quality enhancement mechanism such as GB atom reconstruction, we analyze the time evolution of simulation trajectories. Figures 5(a)–(c) show dislocation

migration between adjacent grains during the electrical current annealing of the sample. Here, we marked two rings at the lower center of the sample by r1 and r2 to track the dislocation position as marked by (⊥) at the GB during different simulation time. Figure 5(a) shows deep yellow colored grain (boundary marked by black dotted line) and its three nearest neighbor grains. Dislocation position adjacent to the ring r2 at the beginning of the annealing simulation is shown in figure 5(a). After 200 ps simulation time this dislocation migrates to the next ring as shown in figure 5(b). The marked dislocation as shown in figure 5(c) further moves to the GB after 975 ps simulation time. This dislocation migration due to effect of electron wind force and Joule heating during electrical current induce annealing could lead to the quality enhancement by reorienting the atoms at the GBs. Figure 5(d) shows a 6|8Mo ring defect at the GB. As mentioned earlier, this ring defect could transform to 6|6|4 defects at the presence of electron wind force and Joule heating. Thus one 6|8Mo ring defect could generate two perfect 6 rings and one 4 ring at the GB site of the sample during the electrical annealing as shown in figures 5(d), (e).

Figure 6 shows the annihilation mechanism of vacancy defects at the GBs of the sample. Here, r1 and r2 rings are marked to track the defects during the simulation. Figure 6(a) shows the vacancy defects at the GBs of the sample in the beginning of the simulation time marked by 0 ps. As the simulation moves forward in time, we notice that vacancy defect (shown in figure 6(a)) transforms to 6|8 S ring defects after 265 ps as shown in figure 6(b). Figure 6(c) shows the intermediate transition of 6|6|4 defects from 6|8 S ring defects after a simulation time of 480 ps. These 6|6|4 defects again transform to 6|8 Mo ring defect after 600 ps as shown in figure 6(d). Thus, dislocation migrates to one ring lower left (figures 6(b) and (d)). After 615 ps of simulation time, 6|8 S ring defects transformed to 6|6|4 defects as shown in figure 6(e). This simulation trajectory analysis shows the mechanism of vacancy defect annihilation at the GBs, which further avails the quality enhancement in the specimen.

To investigate the defect annihilation at the GBs of the MoS_2 specimen, we performed nudged elastic band (NEB) simulation runs using spring constant of 0.5 eV $Å^{-1}$. In our NEB simulation, we use 192 atoms to build both pristine and defective MoS_2 structure as shown in figure 7. In figure 7(d), red dotted lines are used to show our created 4, 8 ring and vacancy defects. As mentioned earlier, these ring-type defects are typical GB defects found in 2D MoS_2 [21, 22]. Figures 7(b)–(d) show the defective structure to pristine structure of MoS_2 conversion during the NEB simulation. Reaction coordinates 0.0 and 1.0 correspond to the pristine and defective structures respectively. The energy barrier plot indicates a defective structure requires approximately 0.8 eV/atom energy to attain a pristine MoS_2 structure. During electrical annealing electrical current could act as an additional stimuli by providing both thermal energy and electron wind force on individual atoms which in turn may overcome this required energy barrier.

4. Conclusion

In this study, we propose that the electron wind force developed during the passage of electrical current can significantly enhance the mobility and migration of defects in 2D MoS_2. Successful validation of this hypothesis implies that electron wind force annealing of MoS_2 specimens with defects (such as GBs in polycrystalline MoS_2) can be achieved at temperatures as low as ambient. This is in stark contrast with the state of the art in 2D MoS_2 annealing, where very high temperatures (~800 °C) are needed. To test our hypothesis, we synthesized monolayer MoS_2 at low temperature (~400 °C) with very good initial crystallinity and room for improvement. We performed *in situ* TEM and classical MD simulation to observe and study the enhancement in the quality of the specimen. The electrical resistance decreased by five times at a dc current density of approximately 9.5×10^5 A cm^{-2}. Such enhanced transport property is supported by the electron wind force induced changes in electron diffraction patterns in regions of specimens where the temperature was constrained to the ambient. In addition to the experiments, we conducted MD simulation to investigate the atomic scale defect migration and grain reconstruction mechanisms that led to specimen quality enhancement. Simulation results shows that during the proposed annealing, the GB atoms could rearrange and reorient due to impetus of electron wind force. NEB calculations show that 6|8, 6|4 and vacancy defects could transform to defect free ring at the expense of external stimuli. This external stimuli could be provided in the form of electrical current (in this study) or thermal energy. To evaluate the effectiveness of the proposed annealing, we also conduct tensile testing of the pre- and post-annealed specimens to show enhancement in mechanical stress-strain properties, which is derived from the elimination of defects and GBs during annealing.

Acknowledgments

We gratefully acknowledge support from the Division of Civil, Mechanical, & Manufacturing Innovation (Nanomanufacturing program) of the National Science Foundation through award No. 1760931.

ORCID iDs

Aman Haque https://orcid.org/0000-0001-6535-5484

References

[1] Mak K F, Lee C, Hone J, Shan J and Heinz T F 2010 Atomically thin MoS_2: a new direct-gap semiconductor *Phys. Rev. Lett.* **105** 136805
[2] Wang Q H, Kalantar-Zadeh K, Kis A, Coleman J N and Strano M S 2012 Electronics and optoelectronics of two-dimensional transition metal dichalcogenides *Nat. Nanotechnol.* **7** 699–712
[3] Xu M S, Liang T, Shi M and Chen H 2013 Graphene-like two-dimensional materials *Chem. Rev.* **113** 3766–98

[4] Novoselov K S, Mishchenko A, Carvalho A and Castro Neto A H 2016 2D materials and van der Waals heterostructures *Science* **353**

[5] Radisavljevic B, Radenovic A, Brivio J, Giacometti V and Kis A 2011 Single-layer MoS_2 transistors *Nat. Nanotechnol.* **6** 147–50

[6] Tong X, Ashalley E, Lin F, Li H and Wang Z M 2015 Advances in MoS_2-based field effect transistors (FETs) *Nano-Micro Lett.* **7** 203–18

[7] Nam H, Oh B R, Chen P, Chen M, Wi S, Wan W, Kurabayashi K and Liang X 2015 Multiple MoS_2 transistors for sensing molecule interaction kinetics *Sci. Rep.* **5** 10546

[8] Cheng R, Jiang S, Chen Y, Liu Y, Weiss N, Cheng H C, Wu H, Huang Y and Duan X 2014 Few-layer molybdenum disulfide transistors and circuits for high-speed flexible electronics *Nat. Commun.* **5** 5143

[9] Pu J, Yomogida Y, Liu K K, Li L J, Iwasa Y and Takenobu T 2012 Highly flexible MoS_2 thin-film transistors with ion gel dielectrics *Nano Lett.* **12** 4013–7

[10] Chang H Y, Yang S, Lee J, Tao L, Hwang W S, Jena D, Lu N and Akinwande D 2013 High-performance, highly bendable MoS_2 transistors with high-K dielectrics for flexible low-power systems *ACS Nano* **7** 5446–52

[11] Li N, Chen X D, Chen X P, Ding X and Zhao X 2017 Ultra-high sensitivity humidity sensor based on MoS_2/Ag composite films *IEEE Electron Device Lett.* **38** 806–9

[12] Yan L R, Shi H, Sui X, Deng Z and Gao L 2017 MoS_2-DNA and MoS_2 based sensors *RSC Adv.* **7** 23573–82

[13] Baugher B W H, Churchill H O H, Yang Y and Jarillo-Herrero P 2013 Intrinsic electronic transport properties of high-quality monolayer and bilayer MoS_2 *Nano Lett.* **13** 4212–6

[14] Choi W, Choudhary N, Han G H, Park J, Akinwande D and Lee Y H 2017 Recent development of two-dimensional transition metal dichalcogenides and their applications *Mater. Today* **20** 116–30

[15] Hong J H *et al* 2015 Exploring atomic defects in molybdenum disulphide monolayers *Nat. Commun.* **6** 6293

[16] Lin Y C *et al* 2018 Realizing large-scale, electronic-grade two-dimensional semiconductors *ACS Nano* **12** 965–75

[17] Nie C B, Yu L, Wei X, Shen J, Lu W, Chen W, Feng S and Shi H 2017 Ultrafast growth of large-area monolayer MoS_2 film via gold foil assistant CVD for a highly sensitive photodetector *Nanotechnology* **28** 275203

[18] Dumitru D *et al* 2015 Large-area epitaxial monolayer MoS_2 *ACS Nano* **9** 4611–20

[19] Jurca T, Moody M J, Henning A, Emery J D, Wang B, Tan J M, Lohr T L, Lauhon L J and Marks T J 2017 Low-temperature atomic layer deposition of MoS_2 films *Angew. Chem.* **129** 5073–7

[20] Fei L, Lei S, Zhang W B, Lu W, Lin Z, Lam C H, Chai Y and Wang Y 2016 Direct TEM observations of growth mechanisms of two-dimensional MoS_2 flakes *Nat. Commun.* **7** 12206

[21] Liu X L, Balla I, Bergeron H and Hersam M C 2016 Point defects and grain boundaries in rotationally commensurate MoS_2 on epitaxial graphene *J. Phys. Chem.* C **120** 20798–805

[22] Zhou W *et al* 2013 Intrinsic structural defects in monolayer molybdenum disulfide *Nano Lett.* **13** 2615–22

[23] Huang P Y *et al* 2011 Grains and grain boundaries in single-layer graphene atomic patchwork quilts *Nature* **469** 389

[24] Yu Q K *et al* 2011 Control and characterization of individual grains and grain boundaries in graphene grown by chemical vapour deposition *Nat. Mater.* **10** 443–9

[25] Najmaei S *et al* 2014 Electrical transport properties of polycrystalline monolayer molybdenum disulfide *ACS Nano* **8** 7930–7

[26] Li X M, Long M Q, Cui L L, Yang K W, Zhang D, Ding J F and Xu H 2016 Effects of line defects on spin-dependent electronic transport of zigzag MoS_2 nanoribbons *AIP Adv.* **6** 015015

[27] Cao A J and Qu J M 2013 Atomistic simulation study of brittle failure in nanocrystalline graphene under uniaxial tension *Appl. Phys. Lett.* **102** 071902

[28] Yasaei P *et al* 2015 Bimodal phonon scattering in graphene grain boundaries *Nano Lett.* **15** 4532–40

[29] Kong D S, Wang H, Cha J J, Pasta M, Koski K J, Yao J and Cui Y 2013 Synthesis of MoS_2 and $MoSe_2$ films with vertically aligned layers *Nano Lett.* **13** 1341–7

[30] Zink N, Therese H A, Pansiot J, Yella A, Banhart F and Tremel W 2008 *In situ* heating TEM study of onion-like WS_2 and MoS_2 nanostructures obtained via MOCVD *Chem. Mater.* **20** 65–71

[31] Reeves C J, Menezes P L, Lovell M R and Jen T C 2013 Tribology of solid lubricants *Tribology for Scientists and Engineers* (Berlin: Springer) pp 447–94

[32] Humphreys F J and H M 2012 *Recrystallization and Related Annealing Phenomena* 2nd edn (Amsterdam: Elsevier) p 658

[33] Conrad H, Sprecher A F, Cao W D and Lu X P 1990 Electroplasticity—the effect of electricity on the mechanical properties of metals *JOM* **42** 28–33

[34] Liang C L and Lin K L 2018 The microstructure and property variations of metals induced by electric current treatment: a review *Mater. Charact.* **145** 545–55

[35] Islam Z, Wang B M and Haque A 2018 Current density effects on the microstructure of zirconium thin films *Scr. Mater.* **144** 18–21

[36] Waryoba D, Islam Z, Wang B and Haque A 2019 Low temperature annealing of metals with electrical wind force effects *J. Mater. Sci. Technol.* **35** 465–72

[37] Plimpton S 1995 Fast parallel algorithms for short-range molecular-dynamics *J. Comput. Phys.* **117** 1–19

[38] Huntington H B and Grone A R 1961 Current-induced marker motion in gold wires *J. Phys. Chem. Solids* **20** 76–87

[39] Lo C L *et al* 2018 Large-area, single-layer molybdenum disulfide synthesized at BEOL compatible temperature as Cu diffusion barrier *IEEE Electron Device Lett.* **39** 873–6

[40] Zhang K *et al* 2018 Considerations for utilizing sodium chloride in epitaxial molybdenum disulfide *ACS Appl. Materi. Interfaces* **10** 40831–7

[41] Haque M A and Saif M T A 2004 Deformation mechanisms in free-standing nanoscale thin films: a quantitative in situ transmission electron microscope study *Proc. Natl Acad. Soc.* **101** 6335–40

[42] Wang B M, Islam Z, Zhang K, Wang K, Robinson J and Haque A 2017 Role of sulphur atoms on stress relaxation and crack propagation in monolayer MoS_2 *Nanotechnology* **28** 365703

[43] Liang T, Phillpot S R and Sinnott S B 2012 Erratum: parametrization of a reactive many-body potential for Mo–S systems (vol 79, 245110, 2009) *Phys. Rev.* B **85** 199903

[44] Sorbello R S, Lodder A and Hoving S J 1982 Finite-cluster description of electromigration *Phys. Rev.* B **25** 6178–87

[45] Bertolazzi S, Brivio J and Kis A 2011 Stretching and breaking of ultrathin MoS_2 *ACS Nano* **5** 9703–9

[46] Young D and Christou A 1994 Failure-mechanism models for electromigration *IEEE Trans. Reliab.* **43** 186–92

[47] Sledzinska M *et al* 2016 Thermal conductivity of MoS_2 polycrystalline nanomembranes *2D Mater.* **3** 035016

[48] Yalon E *et al* 2017 Energy dissipation in monolayer MoS_2 electronics *Nano Lett.* **17** 3429–33

[49] Dutta S, Moors K, Vandemaele M and Adelmann C 2018 Finite size effects in highly scaled ruthenium interconnects *IEEE Electron Device Lett.* **39** 268–71

[50] Thompson C and Smith H I 1984 Surface-energy-driven secondary grain growth in ultrathin (<100 nm) films of silicon *Appl. Phys. Lett.* **44** 603–5

[51] Wu J, Cao P, Zhang Z, Ning F, Zheng S S, He J and Zhang Z 2018 Grain-size-controlled mechanical properties of polycrystalline monolayer MoS_2 *Nano Lett.* **18** 1543–52

[52] van der Zande A M *et al* 2013 Grains and grain boundaries in highly crystalline monolayer molybdenum disulphide *Nat. Mater.* **12** 554–61